Synthetic Multiscale Design of Nanostructured Ni Single Atom Catalyst for Superior CO_2 Electroreduction

Gyoung Hwa Jeong[1,2†], Ying Chuan Tan[3†], Jun Tae Song[4], Gil-Yong Lee[1,2], Ho Jin Lee[1,2], Jaewoong Lim[5], Hu Young Jeong[6], Somi Won[5] and Jihun Oh[2*], Sang Ouk Kim[1,2*]

[1]National Creative Research Initiative (CRI) Center for Multi-Dimensional Directed Nanoscale, KAIST, 291 Daehak-ro, Yuseong-gu, Daejeon 34141, Republic of Korea.

[2]Department of Materials Science and Engineering, KAIST, 291 Daehak-ro, Yuseong-gu, Daejeon 34141, Republic of Korea.

[3]Institute of Materials Research and Engineering (IMRE), A*STAR, 2 Fusionopolis Way, #08-03 Innovis 138634, Singapore.

[4]Department of Applied Chemistry, Faculty of Engineering, Kyushu University, 819-0395 Fukuoka, Japan.

[5]Department of Chemistry, UNIST, 50 UNIST-gil, Ulsan 44919, Republic of Korea.

[6]UNIST Central Research Facilities, UNIST, 50 UNIST-gil, Ulsan 44919, Republic of Korea.

[†]G. H. J. and Y. C. T. contributed equally to this work.

*E-mail: sangouk@kaist.ac.kr and jihun.oh@kaist.ac.kr

Rational design of nanoscale structures can greatly strengthen heterogeneous catalysis with the maximal utilization of active sites. Single atom catalysts (SACs) are recently emerging but a systematic design of nanostructured SAC has rarely been demonstrated yet. Here, distinct architectural structure-dependence of electrochemical CO_2 reduction (CO_2RR) on Ni-based SACs is presented. Starting from Ni-imidazolate coordination polymers (Ni-Im) and their supported counterparts with a carbon nanotube (CNT) and a zeolite imidazolate framework (ZIF-8), the respective derivatives, i.e. Ni-SAC, Ni-SAC-CNT, and Ni-SAC-ZIF8, are obtained after pyrolysis. The presence of substrates ultimately results in large surface porous N-doped carbon nanostructures, which facilitate the diffusion of etchants to remove undesired Ni nanoparticles effectively. The dense Ni single atomic sites contained within the nanostructure are easily accessible to CO_2 reactants during CO_2RR, thus promoting high utilization of active sites even at large current densities. Electro-conductive CNT substrates mediate fluent charge transfer and stimulates the intrinsic activity of catalytic sites. Consequently, operating at 400 mA cm^{-2}, Ni-SAC-CNT attains a high faradaic efficiency of 99 % toward CO at a low overpotential of 0.24 V, equivalent to a record cathodic energetic efficiency and turnover frequency of 83.4 % and 439,000 h^{-1}, respectively.

Keywords: single atom catalyst, CO_2 reduction, carbon nanostructure, electrochemistry

1. Introduction

Rapid advent of environmental issues arising from fossil fuel based current industrial system have triggered intensive research interest in the electrochemical CO_2 reduction reaction (CO_2RR) [1-8]. Among several different electrochemical CO_2RR products, CO is the basic chemical resource for methanol production, Fischer-Tropsch synthetic oils, and various carbonylation reactions [9]. The electrochemical conversion of CO_2 into CO is a typical two-electron process favored at the surface of Au, Ag, and Zn [10, 11]. Nanostructured Au and Ag catalysts with relatively low energy barriers toward CO show excellent electrochemical reduction catalyst activity with CO faradaic efficiency (FE) above 90 % at overpotentials lower than 300 mV [12-14]. Nonetheless, most prior studies have been unable to reach the economical viable activity of 200 mA cm^{-2} particularly due to the limited CO_2 mass transport in a conventional H-type electrochemical cell. Recently, an increasing number of studies have employed flow electrolyzers based on gas-diffusion electrodes (GDEs) to achieve industrially relevant CO production rates [15-17]. Unfortunately, these results still rely on noble metals, which inevitably suffer from a high economic burden for scaling up. Alternatively, efforts have been spent on identifying cheaper alternatives, such as AgZn alloy and Cu/In hybrid [18,19], though they still suffer from high overpotentials and thus large power consumption for electrochemical CO_2RR.

Lately, single atom catalysts (SACs) are emerging as a novel class of catalysts that can be rationally designed for numerous applications, including CO_2RR [20-23]. Among various synthetic methods introduced for SACs thus far [24-29], carbonization of metal organic frameworks (MOFs) have been widely appreciated, motivated from the intrinsic

atomic metal node based framework structures [30-35]. For example, zeolitic imidazolate frameworks (ZIFs) constructed from N-containing organic ligands can be easily transformed into porous N-doped carbons with abundant anchoring sites for single metal atoms. Among the transition-metal SACs anchored on N-doped carbons, Ni-SACs with $Ni^{1+}N_4$ centers have been identified as one of the most active sites for the selective conversion of CO_2 to CO [36,37]. Ni-based ZIFs with 2-methylimidazole (2-MeIm) as the ligand were successfully synthesized by ion-exchange and co-precipitation methods to overcome the inherent poor coordination of Ni^{2+} with 2-MeIm as compared to Zn^{2+} and Co^{2+} [38,39]. Unfortunately, due to the inherent rigid 3-dimensional (3-D) crystal framework of ZIFs, the rational construction of desirable nanostructures has been challenging [40,41]. Furthermore, MOF-derived carbon particles are typically microporous (pore size of less than 2 nm) and readily agglomerate into micrometer-scale structures under high pyrolysis temperature [42]. Therefore, they are likely to encounter under-utilized active sites at high reaction rates arising from the diffusion limitations of reactants and products within the pores [43]. Consequently, Ni-SACs constructed from ZIFs still suffer from high overpotentials for CO_2RR and low levels of metal site utilization, i.e. low values of turnover frequency (TOF; calculated based on total metal content) [38,39].

Based on the limitations of the current ZIF-derived SACs, designing of hierarchical nanostructured SACs is expected to rationally reduce the diffusion lengths and thus fully utilize the active sites. It has been reported that thin layers of (<20 nm thickness) molecular single atom catalytic centers stabilized on substrates have shown superior electrocatalytic properties [37,44,45]. For example, anchoring a monolayer of Ni-based molecular single atom centers on carbon nanotubes (CNTs) was able to achieve one

order of magnitude higher TOF values than the previous reported ZIF-derived SACs [37]. This highlights the importance of maximal exposure of atomically dispersed active sites to the reactant molecules. Obviously, such monolayer of well-defined Ni-SACs provided an insightful model study but should be difficult to attain industrial-relevant current density with the inherent low level of metal content (< 0.3 wt %), i.e. low density of active sites. Consequently, the best CO_2RR catalysts for CO production with practically meaningful activity still rely on nanostructured Au and Ag [15-17].

In this work, we report a direct synthesis of hierarchically structured Ni-imidazolate coordination polymer (Ni-Im) as a precursor for the fabrication of hierarchical nanostructured Ni-SACs. Unlike the 3-D crystalline framework of typical Ni based ZIF, our synthesized Ni-Im exhibits flower-like micro-structures assembled from thin nanoribbons. By introducing multi-functional substrates, such as CNTs, the 1-D ribbon structure readily undergoes structural assembly to form hierarchical nanocomposites (Fig. 1a) [46,47]. After pyrolysis, our optimized CNT-supported SAC (Ni-SAC-CNT) exhibits a large surface area with abundantly exposed Ni single atom active sites desirable for efficient diffusional mass transport as well as a conductive backbone for fluent charge transfer. By utilizing a GDE-based flow electrolyzer, our catalyst attains a record high performance for electrochemical CO_2RR that even surpasses the Au and Ag based catalysts.

2. Experimental

2.1. Materials

Nickel nitrate hexahydrate ($Ni(NO_3)_2 \cdot 6H_2O$, 98%, Alfa), zinc nitrate hexahydrate ($Zn(NO_3)_2 \cdot 6H_2O$, 98%, SAMCHUN), 2-methylimidazole (99%, Sigma-Aldrich), Nafion (5 wt % solution, Sigma-Aldrich), potassium chloride (KCl, > 99.0%), hydrochloric acid (HCl, 37%), and potassium hydroxide (KOH, 99.99%) were used as-received without further purification. Carbon nanotubes (Hanhwa Chemicals) were purified in HCl (7 M) before use. High purity CO_2 gas was used (> 99.999%). Water was purified using a Millipore Milli-Q system (18.2 MΩ·cm).

2.2. Synthesis of Ni-Im, Ni-Im-CNT, Ni-Im-ZIF8.

All pre-catalysts were prepared by aging at 65 ℃ overnight. For the example of Ni-Im, 2 mmol of $Ni(NO_3)_2 \cdot 6H_2O$ and 80 mmol of 2-methylimidazole (2-MeIm) were dissolved in 100 mL methanol. The resultant green solution was kept at 65 ℃ overnight. The final precipitate was yellow. The remaining precursors in solution were removed using ethanol and water. For the hybridization of Ni-Im with CNTs, commercially available CNTs was purified by 7 M HCl treatment. After washing several times with distilled water, the purified CNTs were dried at 95 ℃ overnight. Afterwards, 10 mg of the purified CNTs was dispersed in 100 ml of methanol to form a mixture solution. 2 mmol of $Ni(NO_3)_2 \cdot 6H_2O$ and 80 mmol of 2-MeIm were dissolved in the CNT dispersion. After keeping at 65 ℃ overnight in oven, the olive-green precipitate was washed using ethanol and dried at 80 ℃. For the formation of Ni-Im-ZIF8, the ZIF-8 as a core was synthesized by mixing 16 mmol of $Zn(NO_3)_2 \cdot 6H_2O$ and 32 mmol of 2-MeIm were dissolved in 200 mL methanol. After this solution was kept at room temperature for overnight, the white precipitate was centrifuged and washed with methanol and dried in

oven. The synthesized ZIF-8 was dispersed in 100 mL of methanol and then it is added 2 mmol of $Ni(NO_3)_2 \cdot 6H_2O$ and 80 mmol of 2-MeIm to form Ni-Im as a shell. After keeping at 65 ℃ overnight in oven, the bright-yellow precipitate was washed using ethanol and dried at 80 ℃.

2.3. Synthesis of Ni-SAC, Ni-SAC-CNT, Ni-SAC-ZIF8.

All Ni-Im-based samples were heated to a pre-determined carbonization temperature (600–900 °C) at 6 °C/min under Ar atmosphere. After reaching the target temperature, the samples were held for 2 h, and then cooled to room temperature. The resultant solids were washed in a beaker containing 2 M HCl for 4 h. All catalysts were rinsed with distilled water, and dried at 95 °C overnight.

2.4. Materials Characterizations

High-resolution transmission electron microscopy (HRTEM) and EDS mapping of catalysts were acquired using Talos F200X TEM (FEI company, USA) with 200 kV accelerating voltage. High-angle annular dark-field (HAADF) STEM images were performed using an FEI Titan cubed G2 60-300 kV. Ar adsorption and desorption isotherms were obtained at 87 K on a Micromeritics ASAP 2020 Surface Characterization Analyzer. All samples were activated at 150 ℃ for 6 h prior to the analysis. X-ray photoelectron spectroscopy (XPS) analysis was performed with a multipurpose XPS (Sigma Probe, Thermo VG Scientific, X-ray Source: monochromatic Al K-alpha). XRD patterns were obtained with a Rigaku Ultima IV diffractometer

equipped with a rotating anode and a Cu-Kα radiation source (λ = 0.1541nm). XAS was performed at beamline of 6D of Pohang Accelerator Laboratory.

2.5. Preparation of Catalyst-Loaded Gas Diffusion Electrodes

Ni-SAC/GDE catalyst electrodes were prepared by drop-casting the catalyst ink on the microporous layer (MPL) side of a commercial carbon paper (GDL-39BC, SIGRACET, 2.5×2.5 cm^2). For the preparation of Ni-SAC and Ni-SAC-ZIF8 catalyst ink, 16 mg of the catalyst powder were dispersed in the mixture of 2 mL of ethanol and 100 μL of 5 wt% Nafion solution. For the preparation of Ni-SAC-CNT catalyst ink, 20 mg of the catalyst powder were dispersed in the mixture of 10 mL of dimethylformamide (DMF) and 125 μL of 5 wt% Nafion solution. The catalyst ink was then drop-casted onto the carbon paper placed on a hotplate at 80 °C to yield the total catalyst loading of 0.8 mg cm^{-2}. Noteworthy that the DMF-based ink of Ni-SAC-CNT took ~1 h to dry on the hotplate, which is then transferred to a vacuum oven to dry overnight at 60 °C.

2.6. Electroreduction of CO_2 in a GDE-based Flow Electrolyzer

The electroreduction of CO_2 was conducted in a 3-electrode electrochemical flow cell comprising of cathode and anode chambers separated by an anion-exchange membrane (AEM, Sustainion membrane, Dioxide Materials). Ag/AgCl (saturated KCl) reference electrode (RE-1B, EC-Frontier) and metallic NiFeMo plate as the anode were used unless stated otherwise. The working and counter electrodes had a geometric area

of 2 cm^2 each. All the Ni-SAC cathodes have a total catalyst loading of 0.8 mg cm^{-2}, unless stated otherwise. Commercial Ag/GDE (Dioxide Materials) cathode was used for comparison. During electrochemical measurement, 1.0 M KOH (or as stated in the text/figure) electrolyte was supplied and circulated using a peristaltic pump (Masterflex L/S pump) from 50 mL electrolyte reservoir at 12 mL min^{-1}. To the cathode gas chamber, CO_2 (99.999%) was fed in at 20 sccm (or as stated otherwise) using a mass flow controller (MFC KOREA). The same electrolyte was filled into the anode compartment, which has an opening for O_2 to escape.

Chronopotentiometry measurements were performed with an electrochemical potentiostat (VSP/VMP3B-5, Biologic). Before each electrochemical measurement, a pre-conditioning step was conducted at −10 mA cm^{-2} for 10 min. We found that this step helps to remove residual oxygen within the gas chamber, as well as to create a wetted GDE catalyst layer which we believe could reduce the crossover of gas to the liquid chamber when high current densities are performed. The chronopotentiometry measurements were performed for 20 min for every CO_2RR experiment. During the measurement, solution ohmic resistance was measured *via* electrochemical impedance at 10 min time intervals. At every interval, the ohmic drop was compensated manually (80% *iR*-correction) by subtracting the solution resistance multiplied by the total current from the applied potential. We believe that this step is important because a small change in solution ohmic resistance over time would result in a considerable error in the ohmic drop-compensated potential as the current involved was large. The conversion of the applied electrode potentials (Ag/AgCl scale, $E_{Ag/AgCl}$) to the reversible hydrogen electrode (RHE) scale (E_{RHE}) were carried out with the following equation:

$$E_{\mathrm{RHE}} = E_{\mathrm{Ag/AgCl}} + 0.197 + 0.0591 \cdot pH$$

where the pH value was based on the calculated local pH as reported previously [36,37].

The quantification of gaseous products was performed using the analyses from an on-line gas chromatography (GC, INFICON, 2-channel 3000 Micro GC) equipped with a Plot Q column and a Molsieve 5A column coupled with thermal conductivity detector (TCD). No liquid product from electrocatalysis was detected using HPLC equipped with a SUGAR SH1101 column (Shodex).

The Faradaic efficiencies (FE) for the formation of products (CO and H_2) were calculated using the following equation:

$$\mathrm{FE}_i\ (\%) = \frac{n_i \cdot z_i \cdot F}{Q}$$

where n_i is the amount (mole) of the product (determined from GC analysis) based on the flow rate measured at the outlet stream using an electronic flow meter to account for the decrease in total gas flow rate due to the neutralization reaction between CO_2 and OH^- (not accounting for the decrease in flow rate will cause an overestimated gas product FEs); z_i is the stoichiometric number of electrons consumed to form the product (2 for CO and H_2); F is the Faraday's constant (96485 C mol^{-1}); Q is the amount of charge passed during the time of electrochemical measurement. The CO partial current density was computed by multiplying the CO FE with the total applied current density.

The cathodic energetic efficiency (EE) for the formation of CO was calculated as follows:

$$\mathrm{CO\ Cathodic\ EE}\ (\%) = \frac{1.23\ +\ (-E_{\mathrm{CO}})}{1.23\ +\ (-E_{\mathrm{cathode}})} \times \mathrm{FE}_{\mathrm{CO}}$$

where E_{CO} is the thermodynamic potential of CO_2 reduction to CO (−0.109 V *vs* RHE); $E_{cathode}$ is the applied cathode potential *vs* RHE; FE_{CO} is the CO faradaic efficiency.

The full cell EE for the formation of CO was calculated as follows:

$$\text{CO Full Cell EE (\%)} = \frac{1.23 + (-E_{\text{CO}})}{E_{\text{full cell}}} \times \text{FE}_{\text{CO}}$$

where $E_{\text{full cell}}$ is the applied full cell potential.

The single-pass CO_2 conversion was determined using the following equation:

$$\text{CO}_2 \text{ Conversion (\%)} = \frac{n_{\text{CO}}}{n_{\text{CO}_2,\text{ feed}}} \times 100$$

where $n_{\text{CO2,feed}}$ is the number of moles of CO_2 fed into the electrolyzer (per unit time); n_{CO} is the number of moles of CO produced (per unit time) as detected from GC analysis.

The turnover frequency (TOF) for the formation of CO was calculated as follows:

$$\text{TOF } (\text{h}^{-1}) = \frac{I \cdot \text{FE}_{\text{CO}}/(z \cdot F)}{m_{\text{cat}} \cdot w/M_{\text{Ni}}} \times 3600$$

where I is the total current; FE_{CO} is the CO faradaic efficiency; z is the number of electron transferred for CO production = 2; F is the Faraday's constant (96485 C mol^{-1}); m_{cat} is the mass of catalyst on the 2 cm^2 electrode (0.0016 g if the loading is 0.8 mg cm^{-2}; 0.0002 g if the loading is 0.1 mg cm^{-2}); w is the Ni content (wt%) in the respective Ni-SAC measured from ICP; M_{Ni} is the atomic mass of Ni (58.69 g mol^{-1}).

In order to obtain the Nyquist plot, electrochemical impedance spectroscopy was conducted in a potentiostatic mode at an applied cathodic potential of −1.20 V. CO_2 feed flow rate and electrolyte flow rate were kept the same as described above. The scans were carried out using 100 different frequencies from 10 kHz to 0.1 Hz in logarithmic steps. Single sine wave mode was used for the sweep with a 10 mV wave amplitude. A simplified Randles circuit without the Warburg element was used to fit our data. The double layer capacitance was replaced with a constant phase element (Q) to

approximate the non-ideal behavior of the GDE. The diameter of the semi-circle in the Nyquist plot represents the charge transfer resistance (R_{CT}) in CO_2RR, while the *x*-intercept at high frequency represents the electrolyte resistance (assuming negligible contact resistance). The values of these elements are listed in Supplementary Table S1.

For the stability test, the 3-electrode set-up was used as described above. Chronopotentiometry measurement was performed for 8 h at 200 mA cm^{-2}. CO_2 feed was supplied at 20 sccm, while fresh 1.0 M KOH electrolyte was fed at 1.2 mL min^{-1} to avoid changes in pH or accumulation of carbonate over time.

Full-cell experiments were carried out in a 2-electrode set-up using Ni-SAC-CNT/GDE as the cathode (2 cm^2) and commercial IrO_2/GDE (Dioxide Materials) as the anode (2 cm^2). The cathode and anode were spaced 2 cm apart. No membrane was used, while 3.0 M KOH electrolyte was used in order to reduce the overall cell resistance. CO_2 was fed at 20 sccm and the electrolyte (100 mL reservoir) was circulated at 12 mL min^{-1}. Chronopotentiometry electrolysis were conducted for 20 min for each CO_2RR measurement.

3. Results and Discussion

3.1. Architectural Control of Ni-SACs

Ni^{2+} and 2-MeIm can assemble to form coordination polymers of various morphologies.[48] By increasing the solvothermal temperature, a change in structures from non-uniform spherical agglomerates to web-like nanowires was reported, which was attributed to the change in growth kinetics. Here, we attempted to synthesize Ni-Im

by using a mild temperature (65 °C) and various 2-MeIm to Ni^{2+} molar ratios (see Experimental Procedures). At a low ligand to metal ratio of 10:1, Ni-imidazolate crystallizes in the form of randomly aggregated nanorods with a diameter of ca. 15 nm (Fig. S1, SI). As the 2-MeIm to Ni^{2+} ratio increases to 40:1, the resultant structure exhibits a flower-like morphology of typical diameters around 1–2 um, consisting of thin (10–20 nm) and radially assembled ribbon-like sheets (Fig. 1b, S1c). Powder X-ray diffraction (PXRD) patterns confirm the crystalline state of Ni-Im (Fig. S2, SI), which is consistent to the diffraction patterns from previous report [48] but distinct from those of sodalite ZIF-8 and ZIF-67. Thermogravimetric analysis (TGA) further verifies that Ni-Im has a molecular formula of $Ni(2\text{-MeIm})_2$, which suggests a similar tetrahedral coordination geometry as ZIF-8 and ZIF-67 but with a different long range framework structure (Fig. S3, SI).

The radial growth of nanoribbons to form a flower-like hierarchical structure suggests that the homogeneous nucleation rate is significantly slower than those of heterogeneous nucleation and growth. This formation kinetics is highly advantageous for a hybrid structure formation by exploiting the dominant heterogeneous nucleation and growth at the surfaces of desired substrates. With the introduction of CNT into the reaction mixture, Ni-Im nanoribbons can intimately wrap around the CNT strands to form the hybrid hierarchical structure denoted as Ni-Im-CNT (Fig. 1c,S4,S5).

As shown in Fig. 1d-g, Ni-SAC-CNT structure was obtained after pyrolysis (at 800 ℃ in Ar) and acidic wet etching, where CNT strands are surrounded by ~5 nm diameter carbon onions. The onion-like structure consists of spherical stacking of graphitic multilayers embedded with single atomic Ni sites. Obviously, the atomically dispersed Ni sites were transformed from the Ni nodes of Ni-Im, whereas graphitic

layers originate from the organic ligands (2-MeIm). Energy dispersive X-ray spectroscopy (EDS) elemental mapping analysis of Ni-SAC-CNT presents the well-defined hierarchical structure with C, N, and Ni atoms (Fig. 1f). The high-angle annular dark field scanning transmission electron microscopy (HAADF-STEM) confirmed the presence of Ni atoms (well-dispersed bright dots) at CNTs and carbon onions in Fig. 1g. Notably, wet etching with HCl treatment is important to selectively remove undesirable Ni metal nanoparticles without influencing the single atom sites on the carbon structures. As shown in Fig. 1h, metallic Ni diffraction peaks disappeared after the wet etching process. Furthermore, carbon (002) diffraction peak at 26.2° was converted to a broad peak of oxidized carbon observed around 13.4° (normalized peak, black line). The formation of graphitic carbon was investigated by Raman spectroscopy (Fig. S6). The peaks near 1580 cm^{-1} correspond to the G peak, which represents the presence of planar sp^2 graphitic structures.

When the substrate-free Ni-Im was pyrolyzed under the same condition, the resultant structure (denoted as Ni-SAC) maintained the original flower-like nanoribbon assembly (Fig. S7). However, significant amount of dense Ni nanoparticles was observed, i.e. Ni-SAC consists of both atomic and particulate Ni species. This is attributed to the large aggregated states of nanoribbon, where Ni nodes can readily undergo coalescence at the elevated temperatures. Even after acid treatment, small Ni nanoparticles remain embedded deep inside the carbon matrix (Fig. S7c). By contrast, Ni-SAC-CNT dominantly formed Ni atom sites owing to the low spatial density of Ni-nodes in the surface assembled structure. The Ni-Im nanoribbons at CNT substrates directly transformed into thin porous N-doped carbon layers, which facilitate the access of etchants to dissolve undesired Ni nanoparticles effectively.

Chemical composition and elemental states of Ni-SAC-CNT were investigated by X-ray photoelectron spectroscopy (XPS). The N 1s spectrum was deconvoluted into the peaks for pyridinic (398.77 eV), Ni-N (399.57 eV), pyrrolic (400.33 eV), quaternary (401.17 eV) and oxidized (402.82 eV) N species (Fig. 1i). The Ni-N peak suggests the presence of direct binding of N atoms to Ni atoms [23,49,50].

The composition of Ni atoms in Ni-SAC-CNT was found to be 0.44 at% (2.06 wt%) by XPS. Also, the bonding energy of Ni $2p_{3/2}$ peak was 854.98 eV, which is higher than that of Ni^0 (852.5 eV) and lower than that of Ni^{2+} (853.7 eV), suggesting a valance of Ni species between 0 to +2 (Fig. S8, SI). Fourier transform (FT) k3-weighted $\chi(k)$ function of the extended X-ray adsorption fine structure (EXAFS) spectra exhibited the Ni–N coordination with a peak at 1.42 Å (Fig. 1j). Compared with a pure Ni foil reference, the absence of peak at 2.18 Å indicates no Ni–Ni metallic bond detected in the Ni-SAC-CNT [23,49,50]. The structural parameters of Ni in Ni-SAC-CNT were further quantified through the least-squares curve fitting as shown in Fig S8. According to the fitting, the coordination number of Ni is 3.2, indicating that the Ni atoms mainly have three-fold coordination with N atoms.

For the generality of our synthetic method for Ni-SAC based nanohybrid structures, we demonstrate that MOFs (ZIF-8; metal node: Zn^{2+}, ligand: 2-methylimidazolate) can also be suitable substrates. By replacing CNT with ZIF-8 particles in the same solvothermal conditions, Ni-Im nanoribbons grew selectively at the surface of the MOF substrate via heterogeneous nucleation to form Ni-Im-ZIF8 (Fig. 2a-c). As presented in Fig. 2a, a pyrolysis can carbonize both components (Ni-Im and ZIF-8) to form Ni-SAC nanocomposites (denoted as Ni-SAC-ZIF8, where ZIF8 represents the initial substrate support before pyrolysis), which exhibits sheet-like carbon structures with abundant Ni

single atom sites and chemical states similar to Ni-SAC-CNT (Fig. 2d–h,S9,S10). The binding energy of Ni $2p_{3/2}$ peak from XPS analysis was 855.01 eV close to that of Ni-SAC-CNT (Fig. S8). This result show that the valence of Ni species is usually situated between 0 to +2. Also, the N 1s spectrum emphasizes several N configurations as shown in Fig. 2h. The Ni–N peak at 399.76 eV suggests that these N atoms directly bind to Ni atoms and the binding energy of metal–N is similar to that of Ni–N reported previous results. This observation also agrees well with the aforementioned XPS results. In the EXAFS spectra from Fig. 2i, Ni-SAC-ZIF8 exhibited apparent Ni–N coordination with a peak at 1.63 Å (Fig. 2i). However, it seems that Ni–Ni was still detected, which indicates the presence of remaining Ni NPs even though they were not observed during TEM imaging (Fig 2d-f).

Notably, unlike Ni-SAC-CNT, Zn still remains due to the pyrolysis temperature lower than the boiling point of Zn (ZnO reduction to Zn at 800 ℃ & evaporation of Zn at 907 ℃) (Fig. S8). The amount of Zn is significantly low (0.59 wt%) as compared to the Ni content (5.50 wt%) in XPS analysis. Ni-SAC-CNT and Ni-SAC-ZIF8 have surface areas of 266.46 $m^2 g^{-1}$ and 87.58 $m^2 g^{-1}$, respectively (Fig. S11). It is worth noting that the intrinsic large surface area of ZIF-8 was significantly decreased after pyrolysis in the Ni-SAC-ZIF8, which can be attributed to the agglomeration of N-doped carbon at high temperature [42]. In contrast, Ni-SAC-CNT retains the large surface area while forming additional mesopores that are beneficial for improving diffusional mass transport [42,51]. This suggests 1D CNT substrates are effective in keeping Ni imidazolate polymers physically apart during the pyrolysis and thus minimizing undesired agglomeration.

3.2. Electrochemical CO_2RR Performance of Ni-SACs

Electrochemical performances of our single atom catalysts, including Ni-SAC, Ni-SAC-CNT and Ni-SAC-ZIF8, were investigated in a GDE-based flow cell with 1.0 M KOH catholyte (Fig. 3a). Largely owing to the facilitated CO_2 mass transport compared to H-type or other liquid-phase cells, all the catalysts attain high CO faradaic efficiencies (FE) at the current densities above 200 mA cm^{-2} (Fig. 3b–c, S12). All three Ni-SACs (loading: 0.8 mg cm^{-2}) outperformed commercial Ag catalysts (loading: 1.0 mg cm^{-2}) presenting lower was observed for Ni-SAC at 300 mA cm^{-2}, revealing a CO partial current inferior to Ag catalyst (Fig. 3d). In stark contrast, Ni-SAC-CNT and Ni-SAC-ZIF8 reached 500 and 400 mA cm^{-2}, respectively, while maintaining CO FE over 90 %. Evidently, Ni-SAC-CNT exhibits the best activity among all three Ni-SACs demonstrating the largest CO partial current density with the lowest applied potential.

The significant activation of hydrogen evolution reaction (HER) observed for the Ni-SAC at high overpotential is attributed to the Ni nanoparticles remaining unwashed within the carbon matrix (Fig. S7c). This highlights an important aspect for the optimal design of carbon-based SACs: an easy access of etching solution to remove agglomerated metal particles. As Ni-SAC-CNT and Ni-SAC-ZIF8 were derived from thin layers of Ni-Im shells (< 20 nm), HCl etchants could readily access and dissolve Ni NPs, efficiently. Taking a closer look at the low current density region in Figure 3e, all the Ni-SACs demonstrate similar onset potential levels between −0.149 to −0.170 V vs RHE (reversible hydrogen electrode), which are notably lower than that of commercial Ag with −0.328 V vs RHE. This strongly suggests that the conversion from CO_2 to CO is more kinetically favorable at the atomic Ni sites compared to Ag surfaces. Along with

current density, the differences in performances among three Ni-SACs became more apparent.

Electrochemically active surface area (ECSA) should be the first parameter to consider for the observed electrochemical performances. Obviously, Ni-SAC-CNT and Ni-SAC-ZIF8 have significantly larger ECSA than Ni-SAC (Fig. S13). Upon the normalization against ECSA, Ni-SAC-ZIF8 and Ni-SAC exhibit similar levels of performances at the CO partial current density below 0.4 mA cm^{-2} ECSA (Fig. 4a). In this region, the principal difference in the performances between Ni-SAC-ZIF8 and Ni-SAC in Fig. 3 is due to the difference in ECSA. Significantly, Ni-SAC-CNT shows an apparent performance superior to Ni-SAC-ZIF8 after the ECSA normalization, strongly suggesting additional factors responsible for the enhancement of performance.

Apart from ECSA, atomistic Ni content is another critical parameter for the density of active sites. We compared the turnover frequency (TOF) of all three Ni-SACs, which is a performance metric normalized with the amount of metal content (Fig. 4b). Due to the residual Ni NPs embedded in the carbon support, the Ni content in Ni-SAC is much higher than other catalysts, leading to the TOF values an order of magnitude lower than Ni-SAC-CNT and Ni-SAC-ZIF8. By contrast, Ni-SAC-CNT again presents the best activity in terms of TOF, which can be attributed to a higher utilization of active sites from the short diffusion path length, as well as intrinsically more active catalytic sites.

For the evaluation of the kinetics for CO_2RR with different catalysts, we compared the Tafel slopes (Fig. 4c). Ag catalyst exhibits the Tafel slope of 104 mV dec^{-1}, while all three Ni-SACs show similar lower Tafel slopes of 47–57 mV dec^{-1}, suggesting a quicker kinetics for CO production and a rapid pre-equilibrium electron transfer to form $*CO_2^{\cdot-}$ intermediate [13]. This is consistent to the previous report that highlighted the

role of single-atom low-valent Ni^{+} for the spontaneous charge transfer to CO_2 to form $CO_2^{\delta-}$. This mechanism can reduce the energy barrier for the first electron transfer step in CO_2RR [33,46].

We utilized electrochemical impedance spectroscopy to compare the charge-transfer taking place at the catalyst-electrolyte interfaces (Fig. 4d, Table S1). From the Nyquist plots, clear distinctions are observed. Interestingly, the charge-transfer resistance (R_{CT}) of Ni-SAC-CNT was only 17.3 % while 48.9 % for Ni-SAC and Ni-SAC-ZIF8, respectively. Indeed, Liu *et al.* had observed a more facilitated flow of electrons from the CNT support to NiN_4 moieties [37]. By employing CNT as the conductive support that connects the current collector to the Ni atomic sites, the charge density at these sites could be increased significantly, thus promoting the electron transfer between low-valent Ni^{+} and CO_2 molecules [15,50,52]. This could explain the superior performance of Ni-SAC-CNT as compared to Ni-SAC-ZIF8, which highlights the importance charge-transfer for the structural design of SACs.

3.3. Practical Performance Metrics of Ni-SAC-CNT

Employing our best catalyst, Ni-SAC-CNT, we further explore its performance at practically meaningful conditions. Apart from the catalyst activity, long-term stability is another crucial requirement for the practical applications. Despite the widely recognized high stability of SACs, however, there is no report on the stability of SACs operating at the industry-relevant current density, i.e., 200 mA cm^{-2}, yet [25,53,54]. Such high current densities have been considered challenging due to various factors, such as catalyst deactivation and flooding of gas chamber [15, 55]. In this work, while applying

a constant current density of 200 mA cm^{-2}, the cathodic potential and CO FE were measured to be over 8 h. Under a constant flow of fresh 1.0 M KOH electrolyte at 1.2 mL min^{-1}, we were able to monitor the stability of catalyst, while avoiding the accumulation of carbonates. Surprisingly, Ni-SAC-CNT was able to retain the high CO FE and the applied potential over 8 h continuously without any washing of GDE (Fig. 5a), which highlights the stability of the atomic sites (Fig. S14). By contrast, a significant amount of electrolyte was accumulated in the gas chamber for Ni-SAC after operating longer than 20 min. Along with the increased H_2 FE at high current density for Ni-SAC, gas leakage towards the catholyte chamber was observed. Thus, the extent of flooding could also be affected by the production of H_2, which induces a higher pressure in the gas chamber and thus destabilizes the gas-liquid interface and structural integrity of the GDE.

Recent techno-economic analysis for CO_2RR was done with the assumption of CO_2 conversion of 50 %, which is desirable for the low operation energy costs [56]. Moreover, upon the use of alkaline electrolyte, a high CO_2 conversion would reduce the regeneration cost for hydroxide due to the slow carbonate formation rate from a low average partial pressure of CO_2 in the gas feed. However, such a high conversion rate is rarely reported yet [57-60]. We expect that retaining a high CO FE while achieving high conversion and current density can be extremely difficult due to the low local concentration of CO_2 that can activate H_2 production. Here, while keeping a constant current density of 200 mA cm^{-2}, CO_2 conversion rate for Ni-SAC-CNT was calculated from the variation of CO_2 feed flow rate. As shown in Fig. 5b, reduction of the feed flow rate from 20 to 10 sccm doubled the CO_2 conversion from 13.8 to 27.6 % with the negligible change of CO FE and overpotential. Remarkably, a single-pass CO_2

conversion of 55.0 % was attained at 4 sccm. Although the required overpotential is significantly increased up to 0.535 V, this result is still considerably lower than the required overpotential of commercial Ag catalyst to reach the same current density (200 mA cm^{-2}) at 20 sccm feed flow (0.722 V, Fig. 3b). Noticeably, CO FE is still maintained above 80 %, which highlights the strong affinity of Ni-SAC-CNT for CO_2 that attributes to its superior CO_2RR selectivity.

In a practical application, full cell energetic efficiency (EE) representing the overall efficiency of CO_2RR electrolyzer, is also a significant metric that governs the economic feasibility. Using Ni-SAC-CNT cathode and commercial IrO_2 anode in a two-electrode configuration, we achieved one of the best full cell CO EEs ever reported thus far (Fig. 6a), specifically, 62.2 %, 51.2 %, 43.8 % and 38.2 % at 100, 200, 300 and 400 mA cm^{-2}, respectively. Nonetheless, full cell CO EE is also heavily dependent on other factors, such as anode performance and electrolyzer cell design. By analyzing the components of loss in the full cell EE, major source of the inefficiency was found to originate from the oxygen evolution reaction (OER) overpotential and ohmic drop from solution resistance (Fig. 6b–c, S16, Table S2). OER is known to cause sluggish kinetics arising from the challenging four proton-coupled electron transfers and O-O bond formation. Thus, developing a cheap and efficient OER catalyst is still an important area of research. Another way to reduce the overpotential of anodic reaction and/or compensate for the additional electrical cost is to replace OER with other electrochemical oxidation reactions that produce value-added chemicals [61]. Ohmic drop plays the major contributor for the EE loss in our flow electrolyzer at j_{total} > 200 mA cm^{-2} under the large distance between the two electrodes, even with the use of more concentrated electrolyte (3.0 M KOH). Therefore, a thinner electrochemical cell or zero-gap

membrane electrode assembly (MEA) cell could further enhance the full cell EE of the system.

To provide a meaningful comparison among various CO_2RR catalysts, cathodic EE is another critical evaluation parameter. Unlike full cell EE, cathodic EE does not include the overpotentials from the anode catalyst and the ohmic loss from solution resistance. Owing to the high CO FE and low overpotential, Ni-SAC-CNT achieved an exceptionally high cathodic EE of 88.0 % and 83.4 % for 100 and 400 mA cm^{-2}, respectively. As presented in Fig. 6d (Table S3), these cathodic EE values are the highest even compared to the noble metal catalysts, such as Au and Ag. Also noteworthy that the previous best-performing result exploited excessively concentrated 7.0 M KOH and highly pressured electrochemical cell (7 atm) to enhance the CO_2RR activities [16]. Unfortunately, such harsh reaction conditions could affect the economics of overall system in the industrial scale arising from additional material and operation costs [52]. In the previous CO_2RR studies, long-term stability of electrochemical system has commonly suffered from the irreversible formation of carbonates upon the reaction of KOH electrolyte with CO_2. In this regard, we employed a more stable and cheaper (but less active) electrolyte of 1.0 M $KHCO_3$, in the test for Ni-SAC-CNT (Fig. S16). Surprisingly, the j_{CO} performance and cathodic EE in $KHCO_3$ electrolyte still surpass most of the best previous reports relying on KOH electrolyte (Fig. 6d, S17), thus highlighting the superiority of our catalyst.

In Fig. 6e (Table S4), we compare the TOF of Ni-SAC-CNT with the best performing molecular catalysts and SACs. By reducing the catalyst loading in Ni-SAC-CNT down to 0.1 mg cm^{-2} (Fig. S18), we could successfully improve the TOF, accompanied by a lower mass transfer resistance from the thinner catalyst layer.

Consequently, under 200 mA cm^{-2}, TOF of 246,000 (1.0 M KOH) and 218,000 h^{-1} (1.0 M $KHCO_3$) were achieved at the overpotential of 0.29 and 0.59 V, respectively. At a higher overpotential of 0.70 V in 1.0 M KOH, our catalyst reached the TOF of 439,000 h^{-1}, to the best of our knowledge, which correspond to the record high values (based on the total metal content) ever reported yet.

4. Conclusion

In summary, we succeeded in the direct synthesis of pure Ni-based coordination polymer with thin nanoribbon morphology that can easily assemble at functional substrates (CNT and ZIF-8) to yield hierarchically structured Ni single atom catalysts. Systematic electrochemical characterization clarified that judicious design of catalytic architecture can attain highest catalytic performance for the production of CO *via* CO_2RR. Even under industrially relevant current densities, our Ni-SAC-CNT demonstrated high stability and high single-pass CO_2 conversion with the best cathodic energetic efficiencies and TOFs in both KOH and $KHCO_3$ electrolyte reported to-date. Significantly, a future research direction is suggested to focus on the promotion of CO_2 conversion with minimal performance penalties [5]. Techno-economic analysis could provide further quantification for the ideal optimized conversion rates of various CO_2RR products for the maximized profit as well as minimal carbon emission. As importantly, there is a need to shift away from the reliance of alkaline environment to boost the performance of CO_2 electrolysis. The accumulation of carbonate from the reaction between CO_2 and OH^- would not only result in instability issues in the electrolyzer, additional energy penalties would also be incurred to recover the CO_2 reactant [62, 63]. Therefore, addressing these challenges will further progress CO_2

electrolysis towards industrial relevance.

Acknowledgement

G. H. J. and Y. C. T. contributed equally to this work. This work was supported by the National Creative Research Initiative (CRI) Center for Multi-Dimensional Directed Nanoscale Assembly (2015R1A3A2033061), and funded by the Korean government (Ministry of Science and ICT) through the National Research Foundation (NRF-2017M3D1A1040692 and NRF-2020M3H7A1096388).

Reference

[1] Z. Yin, G.T.R. Palmore, S. Sun, Trends Chem. 1 (2019) 739-750.

[2] J.T. Song, H. Song, B. Kim, J. Oh, Catalysts 9 (2019) 224.

[3] H. Song, M. Im, J.T. Song, J.-A. Lim, B.-S. Kim, Y. Kwon, S. Ryu, J. Oh, Appl. Catal. B-Environ. 232 (2018) 391-396.

[4] S. Nitopi, E. Bertheussen, S.B. Scott, X. Liu, A.K. Engstfeld, S. Horch, B. Seger, I.E.L. Stephens, K. Chan, C. Hahn, J.K. Norskov, T.F. Jaramillo, I. Chorkendorff, Chem. Rev. 119 (2019) 7610-7672.

[5] Y.C. Tan, K.B. Lee, H. Song, J. Oh, Joule 4 (2020) 1104-1120.

[6] H. Song, J.T. Song, B. Kim, Y.C. Tan, J. Oh, Appl. Catal. B-Environ. 272 (2020) 119049.

[7] Y.E. Kim, B. Kim, W. Lee, Y.N. Ko, M.H. Youn, S.K. Jeong, K.T. Park, J. Oh, Chem. Engin. J. 413 (2020) 127448, https://doi.org/10.1016/j.cej.2020.127448.

[8] S. Padmajan Sasikala, G.H. Jeong, T. Yun, S.O. Kim, Energy Storage Mater. 23 (2019) 154-158.

[9] W. Sheng, S. Kattel, S. Yao, B. Yan, Z. Liang, C.J. Hawxhurst, Q. Wu, J.G. Chen, Energy Environ. Sci. 10 (2017) 1180-1185.

[10] Y.S. Ham, S. Choe, M.J. Kim, T. Lim, S.-K. Kim, J.J. Kim, Appl. Catal. B-Environ. 208 (2017) 35-43.

[11] W. Luo, Q. Zhang, J. Zhang, E. Moioli, K. Zhao, A. Züttel, Appl. Catal. B-Environ. 273 (2020) 119060.

[12] S.M. Lee, H. Lee, J. Kim, S.H. Ahn, S.T. Chang, Appl. Catal. B-Environ. 259 (2019) 118045.

[13] M. Liu, Y. Pang, B. Zhang, P. De Luna, O. Voz nyy, J. Xu, X. Zheng, C.T. Dinh,

F. Fan, C. Cao, F.P. de Arquer, T.S. Safaei, A. Mepham, A. Klinkova, E. Kumacheva, T. Filleter, D. Sinton, S.O. Kelley, E.H. Sargent, Nature 537 (2016) 382-386.

[14] G. Hyun, J.T. Song, C. Ahn, Y. Ham, D. Cho, J. Oh, S. Jeon, PNAS 117 (2020) 5680-5685.

[15] S. Verma, Y. Hamasaki, C. Kim, W.X. Huang, S. Lu, H.R.M. Jhong, A.A. Gewirth, T. Fujigaya, N. Nakashima, P.J.A. Kenis, ACS Energy Lett. 3 (2018) 193-198.

[16] C.M. Gabardo, A. Seifitokaldani, J.P. Edwards, C.T. Dinh, T. Burdyny, M.G. Kibria, C.P. O'Brien, E.H. Sargent, D. Sinton, Energy Environ. Sci. 11 (2018) 2531-2539.

[17] B. Kim, H. Seong, J.T. Song, K. Kwak, H. Song, Y.C. Tan, G. Park, D. Lee, J. Oh, ACS Energy Lett. 5 (2019) 749-757.

[18] S. Lamaison, D. Wakerley, J. Blanchard, D. Montero, G. Rousse, D. Mercier, P. Marcus, D. Taverna, D. Giaume, V. Mougel, M. Fontecave, Joule 4 (2020) 395-406.

[19] L. Yan, W. Su, X. Cao, P. Zhang, Y. Fan, Chem. Engin. J. 412 (2021) 128718, https://doi.org/10.1016/j.cej.2021.128718.

[20] Y. Peng, B. Lu, S. Chen, Adv. Mater. 30 (2018) 1801995.

[21] S. Ding, M.J. Hülsey, J. Pérez-Ramírez, N. Yan, Joule 3 (2019) 2897-2929.

[22] W. Bi, X. Li, R. You, M. Chen, R. Yuan, W. Huang, X. Wu, W. Chu, C. Wu, Y. Xie, Adv. Mater. 30 (2018) e1706617.

[23] J. Filippi, L. Rotundo, R. Gobetto, H.A. Miller, C. Nervi, A. Lavacchi, F. Vizza, Chem. Engin. J. 416 (2021) 129050, https://doi.org/10.1016/j.cej.2021.129050.

[24] D.H. Lee, W.J. Lee, W.J. Lee, S.O. Kim, Y.H. Kim, Phys. Rev. Lett. 106 (2011)

175502.

[25] H.-Y. Jeong, M. Balamurugan, V.S.K. Choutipalli, E.-S. Jeong, V. Subramanian, U. Sim, K.T. Nam, J. Mater. Chem. A 7 (2019) 10651-10661.

[26] J. Zhao, J. Deng, J. Han, S. Imhanria, K. Chen, W. Wang, Chem. Engin. J. 389 (2020) 124323, https://doi.org/10.1016/j.cej.2020.124323.

[27] S. Ji, Y. Chen, X. Wang, Z. Zhang, D. Wang, Y. Li, Chem. Rev. 120 (2020) 11900-11955, 10.1021/acs.chemrev.9b00818.

[28] S.A. Abbas, J.T. Song, Y.C. Tan, K.M. Nam, J. Oh, K.D. Jung, ACS Appl. Energy Mater. 3 (2020) 8739-8745.

[29] B. Li, S.P. Sasikala, D.H. Kim, J. Bak, I.-D. Kim, E. Cho, S.O. Kim, Nano Energy 56 (2019) 524-530.

[30] L. Jiao, H.-L. Jiang, Chem 5 (2019) 786-804.

[31] J.H. Lee, Y. Byun, G.H. Jeong, C. Choi, J. Kwen, R. Kim, I.H. Kim, S.O. Kim, H.T. Kim, Adv. Mater. 31 (2019) 1904524.

[32] L. Jiao, R. Zhang, G. Wan, W. Yang, X. Wan, H. Zhou, J. Shui, S.-H. Yu, H.-L. Jiang, Nature Commun. 11 (2020) 2831.

[33] L. Jiao, G. Wan, R. Zhang, X. Zheng, H. Zhou, S.-H. Yu, H.-L. Jiang, Angew. Chem. Int. Ed. Engl. 59 (2020) 20589-20595.

[34] Y.-N. Gong, L. Jiao, Y. Qian, C.-Y. Pan, L. Zheng, X. Cai, B. Liu, S.-H. Yu, H.-L. Jiang, Angew. Chem. Int. Ed. Engl. 59 (2020) 2705-2709.

[35] C. Wang, J. Kim, J. Tang, M. Kim, H. Lim, V. Malgras, J. You, Q. Xu, J. Li, Y. Yamauchi, Chem, 6 (2020), 19-40.

[36] J. Li, P. Pršlja, T. Shinagawa, A.J. Martín Fernández, F. Krumeich, K. Artyushkova, P. Atanassov, A. Zitolo, Y. Zhou, R. García-Muelas, N. López, J.

Pérez-Ramírez, F. Jaouen, ACS Catal. 9 (2019) 10426-10439.

[37] S. Liu, H.B. Yang, S.F. Hung, J. Ding, W. Cai, L. Liu, J. Gao, X. Li, X. Ren, Z. Kuang, Y. Huang, T. Zhang, B. Liu, Angew. Chem. Int. Ed. Engl. 59 (2020) 798-803.

[38] C. Zhao, X. Dai, T. Yao, W. Chen, X. Wang, J. Wang, J. Yang, S. Wei, Y. Wu, Y. Li, J. Am. Chem. Soc. 139 (2017) 8078-8081.

[39] C. Yan, H. Li, Y. Ye, H. Wu, F. Cai, R. Si, J. Xiao, S. Miao, S. Xie, F. Yang, Y. Li, G. Wang, X. Bao, Energy Environ. Sci. 11 (2018) 1204-1210.

[40] Y.C. Tan, H.C. Zeng, Chem. Commun. 52 (2016) 11591-11594.

[41] Y.C. Tan, H.C. Zeng, ChemCatChem 11 (2019) 3138-3165.

[42] C. Hu, S. Bai, L. Gao, S. Liang, J. Yang, S.-D. Cheng, S.-B. Mi, J. Qiu, ACS Catal. 9 (2019) 11579-11588.

[43] X. Zhang, D. Liu, D. Xu, S. Asahina, K.A. Cychosz, K.V. Agrawal, Y. Al Wahedi, A. Bhan, S. Al Hashimi, O. Terasaki, M. Thommes, M. Tsapatsis, Science 336 (2012) 1684-1687.

[44] N. Han, Y. Wang, L. Ma, J. Wen, J. Li, H. Zheng, K. Nie, X. Wang, F. Zhao, Y. Li, J. Fan, J. Zhong, T. Wu, D.J. Miller, J. Lu, S.-T. Lee, Y. Li, Chem 3 (2017) 652-664.

[45] M. Wang, K. Torbensen, D. Salvatore, S. Ren, D. Joulie, F. Dumoulin, D. Mendoza, B. Lassalle-Kaiser, U. Isci, C.P. Berlinguette, M. Robert, Nat. Commun. 10 (2019) 3602.

[46] U.N. Maiti, W.J. Lee, J.M. Lee, Y. Oh, J.Y. Kim, J.E. Kim, J. Shim, T.H. Han, S.O. Kim, Adv. Mater. 26 (2014) 40-66.

[47] G.H. Jeong, S.P. Sasikala, T. Yun, G.Y. Lee, W.J. Lee, S.O. Kim, Adv. Mater. 32

(2020) 1907006.

[48] M. Yuan, R. Wang, Z. Sun, L. Lin, H. Yang, H. Li, C. Nan, G. Sun, S. Ma, Inorg. Chem. 58 (2019) 11449-11457.

[49] K. Jiang, S. Siahrostami, T.T. Zheng, Y.F. Hu, S. Hwang, E. Stavitski, Y.D. Peng, J. Dynes, M. Gangisetty, D. Su, K. Attenkofer, H.T. Wang, Energy Environ. Sci. 11 (2018) 893-903.

[50] H.B. Yang, S.F. Hung, S. Liu, K.D. Yuan, S. Miao, L.P. Zhang, X. Huang, H.Y. Wang, W.Z. Cai, R. Chen, J.J. Gao, X.F. Yang, W. Chen, Y.Q. Huang, H.M. Chen, C.M. Li, T. Zhang, B. Liu, Nat. Energy 3 (2018) 140-147.

[51] Y.C. Tan, H.C. Zeng, Adv. Funct. Mater. 27 (2017) 1703765.

[52] S.C. Ma, R. Luo, J.I. Gold, A.Z. Yu, B. Kim, P.J.A. Kenis, J. Mater. Chem. A 4 (2016) 8573-8578.

[53] M. Wang, L. Chen, T.C. Lau, M. Robert, Angew. Chem. Int. Ed. 57 (2018) 7769-7773.

[54] T. Zheng, K. Jiang, N. Ta, Y. Hu, J. Zeng, J. Liu, H. Wang, Joule 3 (2019) 265-278.

[55] J.J. Lv, M. Jouny, W. Luc, W. Zhu, J.J. Zhu, F. Jiao, Adv. Mater. 30 (2018) e1803111.

[56] M. Jouny, W. Luc, F. Jiao, Ind. Eng. Chem. Res. 57 (2018) 2165-2177.

[57] T. Haas, R. Krause, R. Weber, M. Demler, G. Schmid, Nat. Catal., 1 (2018) 32-39.

[58] C.T. Dinh, Y.G.C. Li, E.H. Sargent, Joule 3 (2019) 13-15.

[59] B. Endrodi, E. Kecsenovity, A. Samu, F. Darvas, R.V. Jones, V. Torok, A. Danyi, C. Janaky, ACS Energy Lett. 4 (2019) 1770-1777.

[60] B.U. Choi, Y.C. Tan, H. Song, K. B. Lee, J. Oh, ACS Sustain. Chem. Engin. 9

(2021) 2348-2357.

[61] S. Verma, S. Lu, P.J.A. Kenis, Nat. Energy 4 (2019) 466-474.

[62] J.A. Rabinowitz, M.W. Kanan, Nat. Commun. 11 (2020), 5231.

[63] C. Chen, Y. Li, P. Yang, Joule *5* (2021), 737-742.

Figure captions

Fig. 1 a) Schematic illustration of the synthesis of Ni-SAC-CNT. b) TEM image of Ni-Im before pyrolysis. c-e) HR-TEM images, f) elemental mapping images, and g) STEM images of Ni-SAC-CNT. h) XRD patterns of Ni-SAC-CNT before (red) and after acid treatment (black). i) N 1s XPS spectra of Ni-SAC-CNT after acid treatments. Atomic contents of N species including pyridinic N, pyrrolic N, graphitic N, and Ni metallic N. j) Fourier transformations of EXAFS spectra for Ni-SAC-CNT.

Fig. 2 a) Schematic illustration of the synthesis of Ni-SAC-ZIF8. b,c) TEM images and elemental mapping images of Ni-SAC-ZIF8 before pyrolysis. d) HR-TEM image of Ni-SAC-ZIF8. e,f) STEM images of Ni-SAC-ZIF8. g) XRD patterns of various Ni-SAC-ZIF8 before (red) and after acid treatment (black). h) N 1s XPS spectra of Ni-SACs after acid treatments. Atomic contents of N species including pyridinic N, pyrrolic N, graphitic N, and Ni metallic N. i) Fourier transformations of EXAFS spectra for Ni-SAC-ZIF8.

Fig. 3 a) Simplified illustration of the GDE-based CO_2 electroreduction system (left) and the GDE components (right); gas diffusion layer (GDL), microporous layer (MPL), and catalyst layer. b) Total current density (j_{total}), c) CO faradaic efficiency, and d,e) CO partial current density (j_{CO}) as a function of cathodic potential in 1.0 M KOH electrolyte. Error bars represent the standard deviations of three separate measurements.

Fig. 4 Comparison of electrochemical properties of the different Ni-SACs. a) j_{CO} normalized to the electrochemically active surface area (ECSA) as a function of cathodic potential, b) turnover frequency (TOF) as a function of cathodic overpotential. Note that the TOF values are calculated based on the total Ni content measured from ICP, as described in

the experimental section. c) Tafel slopes of different catalysts for the electrochemical reduction of CO_2 to CO, and d) Nyquist plot attained from electrochemical impedance spectroscopy at a cathodic potential of −1.2 V vs Ag/AgCl. All electrochemical measurements displayed here are carried out in 1.0 M KOH electrolyte.

Fig. 5 a) Stability test of Ni-SAC-CNT at a constant total current density of 200 mA cm^{-2} with cathodic potential and CO faradaic efficiency plotted as a function of time. b) Plot of CO_2 conversion, CO faradaic efficiency and cathodic overpotential as a function of CO_2 feed flow rate at a constant total current density of 200 mA cm^{-2}.

Fig. 6 a) Comparison of the full cell energetic efficiency as a function of total current density. b) Plot of applied voltage breakdown as a function of total current density. c) Plot of components constituting to the loss of energetic efficiency as a function of total current density. d) Comparison of cathodic energetic efficiency as a function of j_{total} for electrocatalytic systems using GDE-based flow cells; note that only representative literatures exhibiting current densities over 100 mA cm^{-2} are shown. e) Comparison of TOF as a function of overpotential with other molecular or atomically dispersed catalysts. Refer to Table S2–S4, Supporting Information for a more detailed comparison and references.

Fig.1

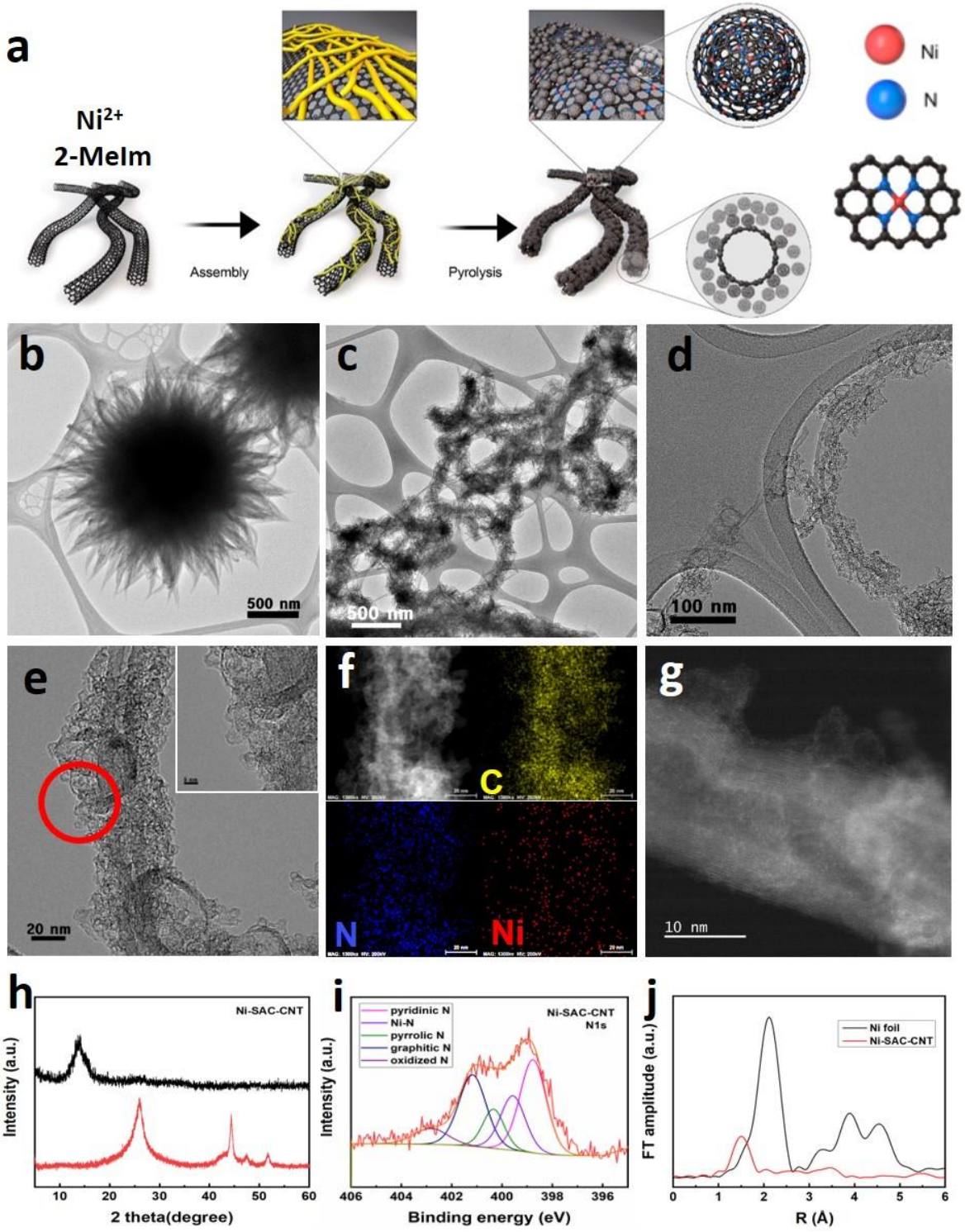
a
Ni2+
2-MeIm
Assembly
Pyrolysis
Ni
N
b
500 nm
c
500 nm
d
100 nm
e
20 nm
f
C
N
Ni
g
10 nm
h
Ni-SAC-CNT
Intensity (a.u.)
2 theta(degree)
i
pyridinic N
Ni-N
pyrrolic N
graphitic N
oxidized N
Ni-SAC-CNT
N1s
Intensity (a.u.)
Binding energy (eV)
j
Ni foil
Ni-SAC-CNT
FT amplitude (a.u.)
R (Å)

Fig.2

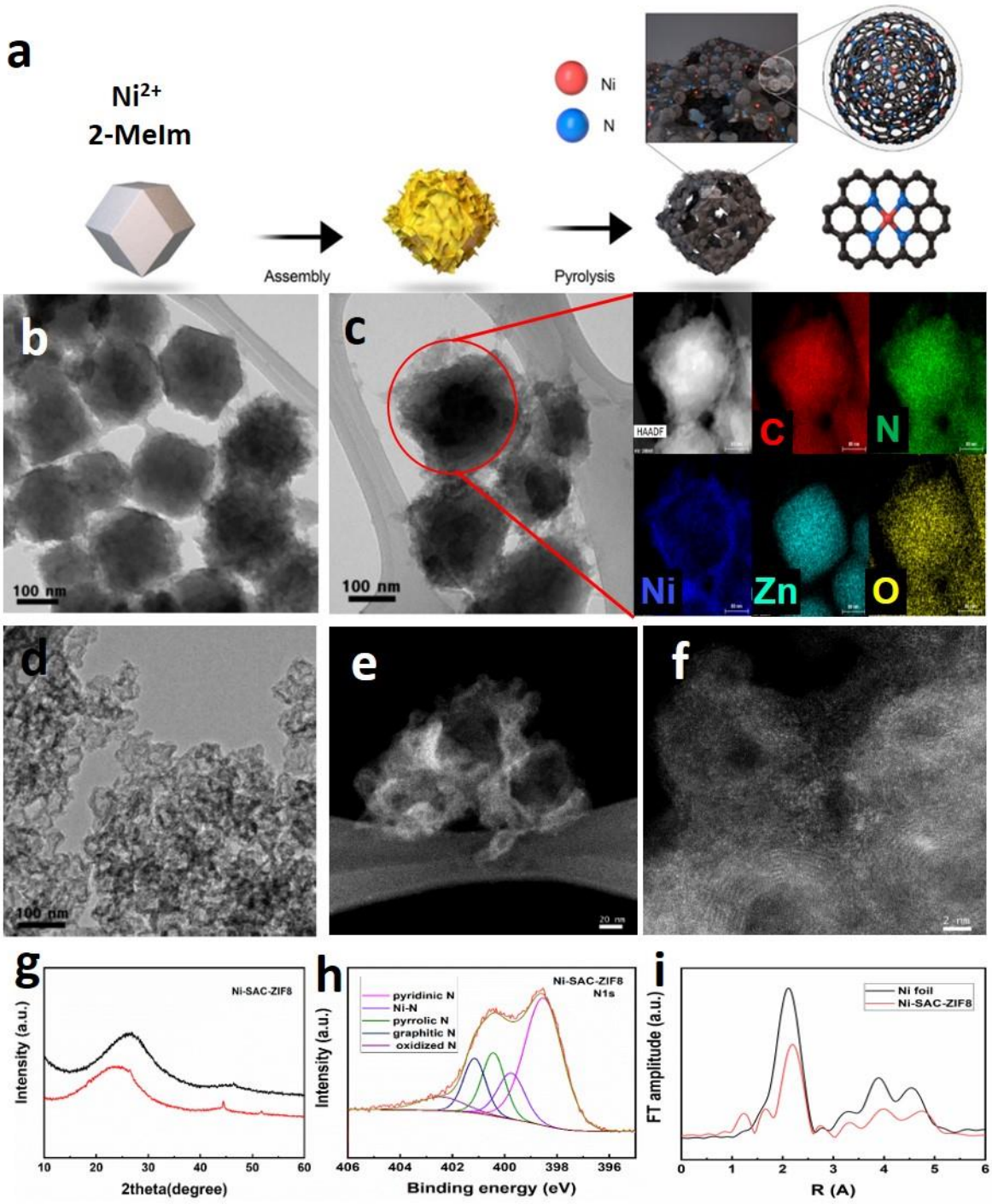
a
Ni2+
2-MeIm
Ni
N
Assembly
Pyrolysis
b
100 nm
c
100 nm
HAADF
C
N
Ni
Zn
O
d
100 nm
e
20 nm
f
2 nm
g
Ni-SAC-ZIF8
Intensity (a.u.)
10 20 30 40 50 60
2theta(degree)
h
Ni-SAC-ZIF8
N1s
pyridinic N
Ni-N
pyrrolic N
graphitic N
oxidized N
Intensity (a.u.)
406 404 402 400 398 396
Binding energy (eV)
i
Ni foil
Ni-SAC-ZIF8
FT amplitude (a.u.)
0 1 2 3 4 5 6
R (A)

Fig. 3

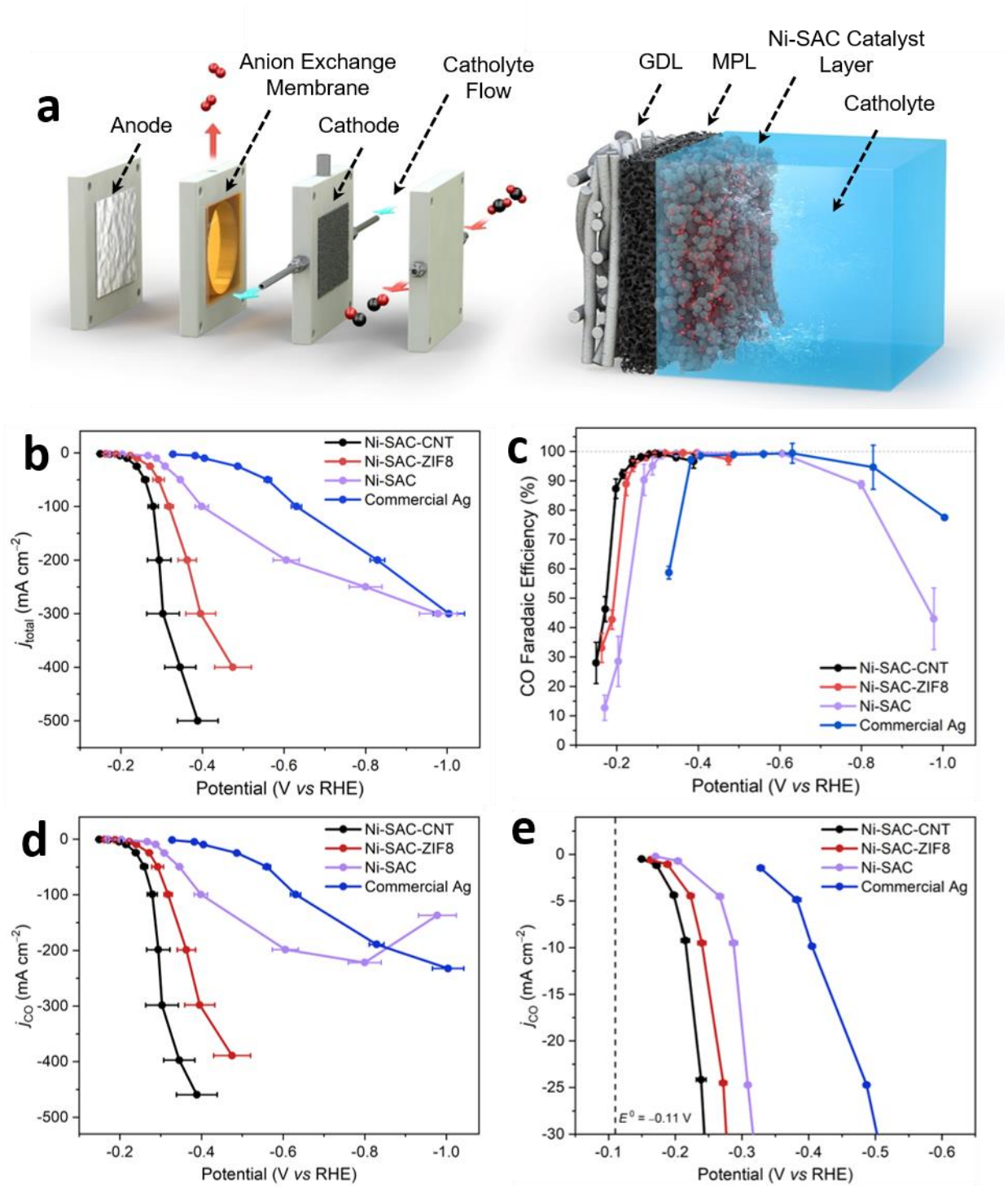
a
Anode
Anion Exchange Membrane
Cathode
Catholyte Flow
GDL
MPL
Ni-SAC Catalyst Layer
Catholyte
b
Ni-SAC-CNT
Ni-SAC-ZIF8
Ni-SAC
Commercial Ag
j_{total} (mA cm^{-2})
Potential (V vs RHE)
c
CO Faradaic Efficiency (%)
Potential (V vs RHE)
d
j_{CO} (mA cm^{-2})
Potential (V vs RHE)
e
j_{CO} (mA cm^{-2})
E^0 = -0.11 V
Potential (V vs RHE)

Fig. 4

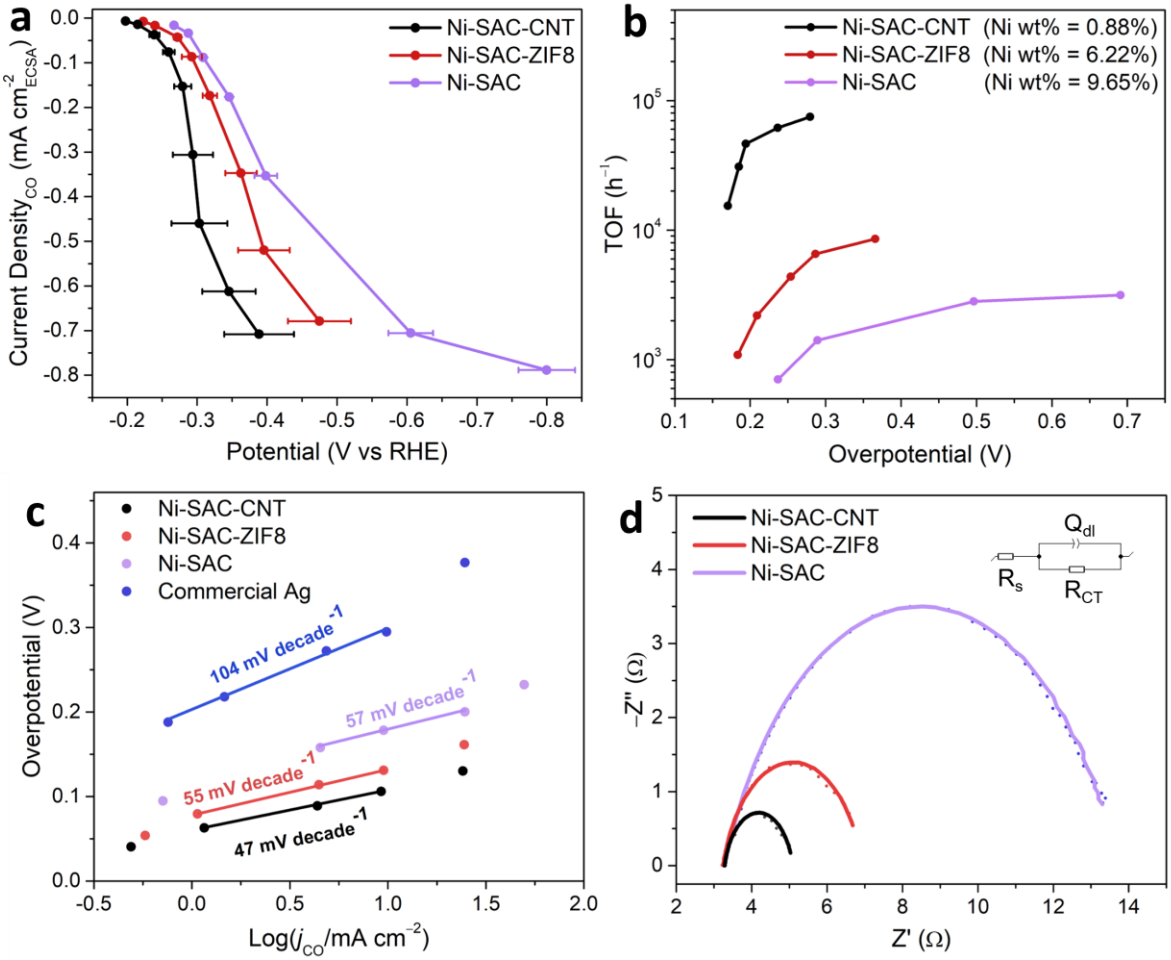
a
Ni-SAC-CNT
Ni-SAC-ZIF8
Ni-SAC
Current Density$_{CO}$ (mA cm$^{-2}_{ECSA}$)
Potential (V vs RHE)
b
Ni-SAC-CNT (Ni wt% = 0.88%)
Ni-SAC-ZIF8 (Ni wt% = 6.22%)
Ni-SAC (Ni wt% = 9.65%)
TOF (h^{-1})
Overpotential (V)
c
Ni-SAC-CNT
Ni-SAC-ZIF8
Ni-SAC
Commercial Ag
104 mV decade^{-1}
57 mV decade^{-1}
55 mV decade^{-1}
47 mV decade^{-1}
Overpotential (V)
Log(j_{CO}/mA cm^{-2})
d
Ni-SAC-CNT
Ni-SAC-ZIF8
Ni-SAC
Q_{dl}
R_s
R_{CT}
-Z'' (Ω)
Z' (Ω)

Fig. 5

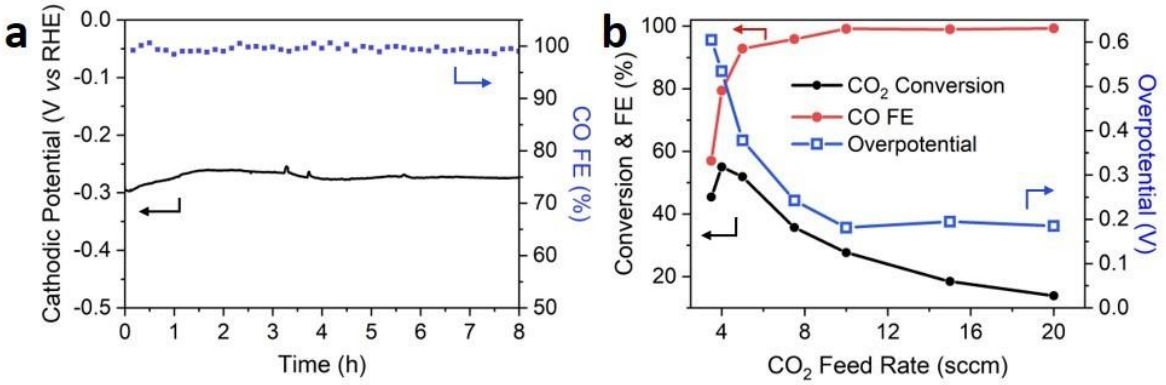
a
Cathodic Potential (V vs RHE)
0.0
-0.1
-0.2
-0.3
-0.4
-0.5
0
1
2
3
4
5
6
7
8
Time (h)
100
90
80
70
60
50
CO FE (%)
b
Conversion & FE (%)
100
80
60
40
20
4
8
12
16
20
CO2 Feed Rate (sccm)
CO2 Conversion
CO FE
Overpotential
0.6
0.5
0.4
0.3
0.2
0.1
0.0
Overpotential (V)

Fig. 6

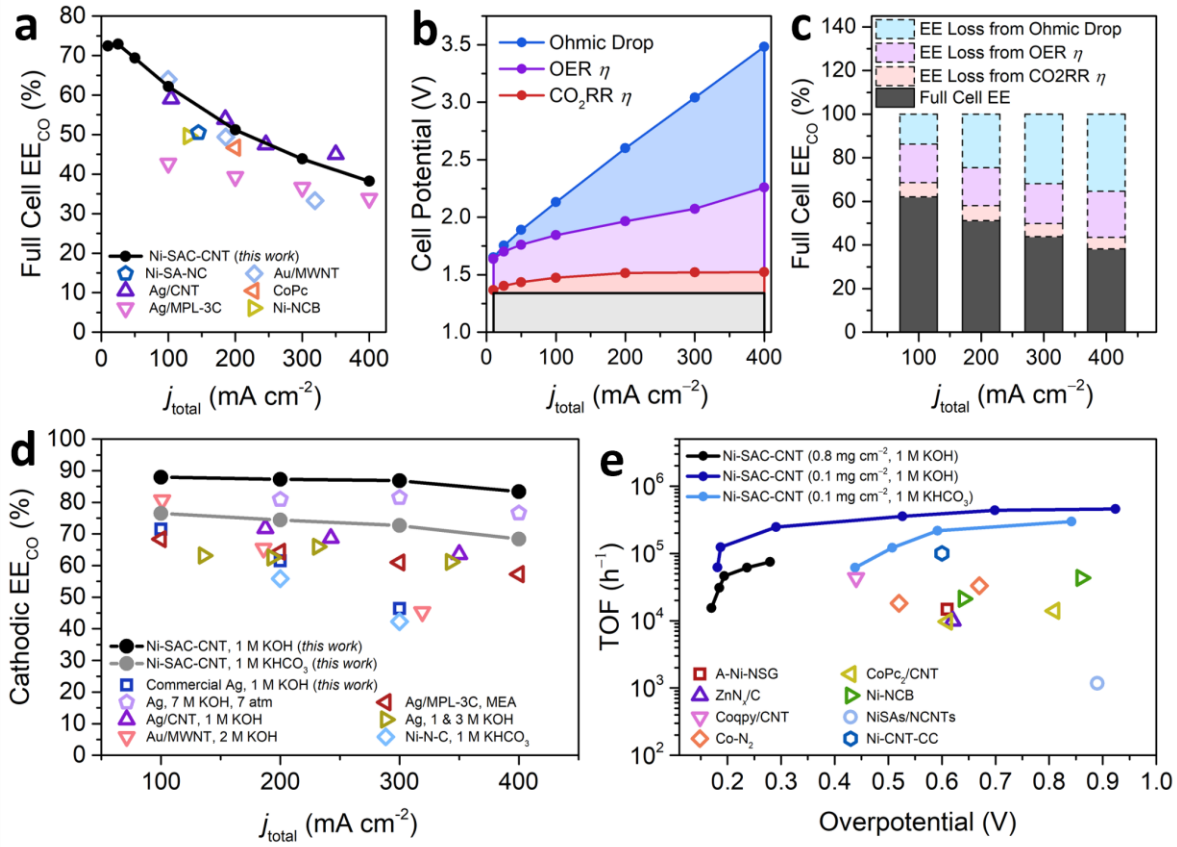
a
Full Cell EE$_{CO}$ (%)
j_{total} (mA cm^{-2})
Ni-SAC-CNT (this work)
Ni-SA-NC
Au/MWNT
Ag/CNT
CoPc
Ag/MPL-3C
Ni-NCB
b
Cell Potential (V)
Ohmic Drop
OER η
CO$_2$RR η
j_{total} (mA cm^{-2})
c
Full Cell EE$_{CO}$ (%)
EE Loss from Ohmic Drop
EE Loss from OER η
EE Loss from CO2RR η
Full Cell EE
j_{total} (mA cm^{-2})
d
Cathodic EE$_{CO}$ (%)
Ni-SAC-CNT, 1 M KOH (this work)
Ni-SAC-CNT, 1 M KHCO$_3$ (this work)
Commercial Ag, 1 M KOH (this work)
Ag, 7 M KOH, 7 atm
Ag/MPL-3C, MEA
Ag/CNT, 1 M KOH
Ag, 1 & 3 M KOH
Au/MWNT, 2 M KOH
Ni-N-C, 1 M KHCO$_3$
j_{total} (mA cm^{-2})
e
Ni-SAC-CNT (0.8 mg cm^{-2}, 1 M KOH)
Ni-SAC-CNT (0.1 mg cm^{-2}, 1 M KOH)
Ni-SAC-CNT (0.1 mg cm^{-2}, 1 M KHCO$_3$)
TOF (h^{-1})
A-Ni-NSG
ZnN$_x$/C
Coqpy/CNT
Co-N$_2$
CoPc$_2$/CNT
Ni-NCB
NiSAs/NCNTs
Ni-CNT-CC
Overpotential (V)